

See discussions, stats, and author profiles for this publication at: <https://www.researchgate.net/publication/228633534>

Effect of Blade Speed on Granular Flow and Mixing in a Cylindrical Mixer

ARTICLE *in* INDUSTRIAL & ENGINEERING CHEMISTRY RESEARCH · JUNE 2010

Impact Factor: 2.59 · DOI: 10.1021/ie901581t

CITATIONS

15

READS

92

4 AUTHORS, INCLUDING:



Aibing Yu

University of New South Wales

623 PUBLICATIONS 11,730 CITATIONS

SEE PROFILE

Effect of Blade Speed on Granular Flow and Mixing in a Cylindrical Mixer

G. R. Chandratilleke,[†] Y. C. Zhou,[†] A. B. Yu,^{*,†} and J. Bridgwater[‡]

Laboratory for Simulation and Modeling of Particulate Systems, School of Materials Science and Engineering, University of New South Wales, Sydney, NSW 2052, Australia, and Department of Chemical Engineering, University of Cambridge, Pembroke Street, Cambridge CB2 3RA, United Kingdom

The discrete element method (DEM) offers the possibility of understanding mixing processes at a microscopic, particle level. In connection with previous studies, DEM is used in this work to investigate the mixing of monosized spherical particles with blade speeds in the range 2–100 rpm. Recirculating flows are observed in both horizontal and cylindrical sections of the bed, providing a mixing mechanism. The recirculating flows formed in front of the blade in cylindrical sections seem to disappear, bringing a reduction of mixing rate at high blade speeds. Viewed at the particle scale, a zone of large interparticle forces is present in front of the blade, and this zone moves toward the vessel walls at high speeds. These are the regions where particle breakage or fracture can happen. Interparticle forces in the bed as a whole increase with the blade speed. Moreover, particle mixing has been studied at both macroscopic and particle scales using conventional mixing index and coordination or contact numbers. One conventional mixing index shows a slight reduction in mixing rate in the transition mixing region up to a certain blade speed and a slight improvement thereafter. This improvement is probably caused by the toroidal motion of particles induced at high blade speeds. Coordination number is successful in capturing the mixing process, and indicates a new way of studying particle-scale mixing.

Introduction

The mixing of granular materials is a vital operation in the manufacture of many types of products and, as a result, has been a focus of research for many years.^{1–3} However, many of such studies are on the macroscopic or global scale, with the resulting information often being useful only for understanding an operation of particular interest. Lack of quantitative and fundamental understanding of mixing processes makes it difficult to address issues such as design, scale-up, and control of mixing processes of various types in a general way. Particle-scale research has been recognized as a promising approach to overcome this difficulty. In the past, such research has been carried out by experiments, first by “freezing” the beds and subsequently dissecting them; this process is laborious and suffers from large errors.^{4,5} Recent studies are mainly based on newly developed experimental and numerical techniques, most notable among which are the method of positron emission particle tracking (PEPT)^{6,7} and the discrete element method (DEM).⁸

In PEPT experiments, the trajectories of some tracer particles are used to determine the flow field of particles in a particle system. By contrast, a DEM simulation can not only generate trajectories of all the particles in a system, but also provide such particle-scale information as transient forces acting on particles. Such information is invaluable for assessing fundamentals governing the motion of particles in mixing systems. Advantages and disadvantages of the two methods have been discussed by Zhou et al.⁹ and Stewart et al.¹⁰ According to the authors, the two methods are complementary: PEPT results can be used to validate and improve DEM based models and, conversely, DEM models can be used to evaluate a range of parameters and to provide information on the microscopic behavior and structure. DEM is thus a valuable tool, and coupled with carefully selected

experiments it can generate rich information from particle scale to process equipment scale. Such studies about the flow and performance should provide an understanding of many of the problems debilitating the discipline, thus helping to secure the underlying science needed for design and operational purposes in practice.

Mixers used in industry are diverse; the type of mixer to be used and its operational conditions are dependent upon the intended application. For example, in the pharmaceutical industry, bladed mixers are used for mixing and granulation of powders. Such operations need to be carried out at appropriate blade speeds to obtain necessary quality and maximum throughput. However, a change in the blade speed will bring about changes to the mixing process in many ways. For example, there will be changes in the particle flow patterns, particle structure, and forces imparted to the particles in the mixture. Knowledge of these matters is still in its infancy. In addition, investigation of the effect of blade speed will also become important when scaling down a mixer in an attempt to study a full-scale mixer. For example, if a small-scale mixer is to operate under operational conditions similar to those of the full-scale mixer, the blades should rotate at a higher speed in the scaled-down mixer according to a relationship between dimensionless blade torque and the Froude number developed by Knight et al.¹¹ Therefore, when investigating the effect of blade speed at the full scale, the rotational speeds at the reduced scale should be varied over a wider range, preferably by at least 2 orders of magnitude.

Here, a DEM is used to simulate the particle flow and mixing in a vertical cylindrical mixer with an axial shaft fitted with two flat blades, with special reference to the effect of rotational speed. Such mixers find use in industrial applications as granular driers or as high-speed granulators and mixers. More importantly, this mixer captures the essential features of an actual mixing process and provides a simple enough configuration for studying the fundamental processes. This system has therefore

* To whom correspondence should be addressed. Fax: 61 2 9385 5965. E-mail: a.yu@unsw.edu.au.

[†] University of New South Wales.

[‡] University of Cambridge.

Table 1. Formulas for Contact Forces and Torques

forces and torques	formula	associated definitions
normal contact force	$\mathbf{F}_{cn,ij} = -\frac{E}{3(1-\nu^2)}(2R_i)^{1/2}\delta_n^{3/2}\hat{\mathbf{n}}$	$\hat{\mathbf{n}} = \frac{\mathbf{R}_i}{R_i}$
normal damping force	$\mathbf{F}_{dn,ij} = -c_n \left(\frac{3m_i E}{\sqrt{2}(1-\nu^2)} (R\delta_n)^{1/2} \right)^{1/2} (\mathbf{V}_{ij} \cdot \hat{\mathbf{n}}) \hat{\mathbf{n}}$	$\mathbf{V}_{ij} = \mathbf{V}_j - \mathbf{V}_i + \boldsymbol{\omega}_j \times \mathbf{R}_j - \boldsymbol{\omega}_i \times \mathbf{R}_i$
tangential contact force	$\mathbf{F}_{ct,ij} = -\frac{\mu_s F_{cn,ij}}{ \boldsymbol{\delta}_t } \left[1 - \left\{ 1 - \frac{\min(\boldsymbol{\delta}_t , \delta_{t,max})}{\delta_{t,max}} \right\}^{3/2} \right] \boldsymbol{\delta}_t$	$\delta_{t,max} = \mu_s \frac{2-\nu}{2(1-\nu)} \delta_n$
tangential damping force	$\mathbf{F}_{dt,ij} = -c_t \left(6m_i \mu_s F_{cn,ij} \frac{\sqrt{1-\delta_t/\delta_{t,max}}}{\delta_{t,max}} \right)^{1/2} \mathbf{V}_{t,ij}$	$\mathbf{V}_{t,ij} = (\mathbf{V}_{ij} \times \hat{\mathbf{n}}) \times \hat{\mathbf{n}}$
rotational torque	$\mathbf{T}_{ij} = \mathbf{R}_i \times (\mathbf{F}_{ct,ij} + \mathbf{F}_{dt,ij})$	
rolling friction torque	$\mathbf{M}_{ij} = -\mu_r F_{cn,ij} \hat{\boldsymbol{\omega}}_i$	$\hat{\boldsymbol{\omega}}_i = \frac{\boldsymbol{\omega}_i}{\omega_i}$

been the focus of several studies.^{9,10} From this point of view, the work reported here is an extension of the previous studies.

Numerical Method

DEM Simulation. The DEM model used here was developed previously,^{9,12} extending the original DEM model proposed by Cundall and Strack⁸ by accounting for the rolling friction of particles. The model uses two momentum conservation equations to describe the translational and rotational motion of particle *i* in a system at time *t* subjected to the gravity and interactions with the neighboring particles, blade, and walls:

$$m_i \frac{d\mathbf{V}_i}{dt} = m_i \mathbf{g} + \sum_{j=1}^{k_i} (\mathbf{F}_{c,ij} + \mathbf{F}_{d,ij}) \quad (1)$$

and

$$I_i \frac{d\boldsymbol{\omega}_i}{dt} = \sum_{j=1}^{k_i} (\mathbf{T}_{ij} + \mathbf{M}_{ij}) \quad (2)$$

Here m_i , I_i , \mathbf{V}_i , and $\boldsymbol{\omega}_i$ are the mass, moment of inertia, translational velocity, and rotational velocity of the particle, respectively. k_i is the number of particles that are in contact with particle *i*. \mathbf{F}_c represents the elastic contact force, which is the summation of the normal and tangential forces $\mathbf{F}_{cn,ij}$ and $\mathbf{F}_{ct,ij}$ respectively at the contact point with particle *j*. \mathbf{F}_d represents the damping force, which is the summation of the normal and tangential damping forces $\mathbf{F}_{dn,ij}$ and $\mathbf{F}_{dt,ij}$ respectively at the

contact point with particle *j*. \mathbf{T}_{ij} and \mathbf{M}_{ij} are the torque and rolling friction torque on particle *i* due to particle *j*, respectively. The equations for the calculation of the forces and torques in eqs 1 and 2 are given in Table 1. They are commonly used as discussed in the recent review of various force models for DEM simulations.¹³

Simulation Conditions. The mixer geometry and simulation conditions are very similar to those in a PEPT study by Stewart et al.¹⁰ The mixer consists of a vertical cylindrical vessel and two flat blades, which are attached to an axial shaft along a diameter of the vessel as shown in Figure 1a. The mixer vessel has an inner diameter of 0.249 m, and the axial shaft of the mixer has a diameter of 0.032 m. The blades are each 0.04 m in height and 0.010 m in thickness; the blades have no clearance either at the cylindrical wall or at the bottom of the vessel.

The particles are considered to be spherical with properties close to those of glass beads. In addition, the walls of the mixer and blades are assumed to have properties that are identical to those of the particles. The physical properties used in the simulation are the following: rolling friction coefficient, $\mu_r = 5 \times 10^{-5}$ m; sliding friction coefficient, $\mu_s = 0.3$; particle density, $\rho = 2500 \text{ kg/m}^3$; Poisson's ratio, $\nu = 0.3$; and damping coefficients, c_n and $c_t = 0.3$. Young's modulus *E*, however, was reduced from 10^9 of real glass beads to 2.16×10^6 to reduce computational time; this approach has been found to be able to produce reliable results.^{9,12} The time step used is 5×10^{-6} s.

A simulation is started with a random placement of 16 000 monosized spheres of 5 mm diameter in the mixer without allowing particles to overlap. This particle generation process

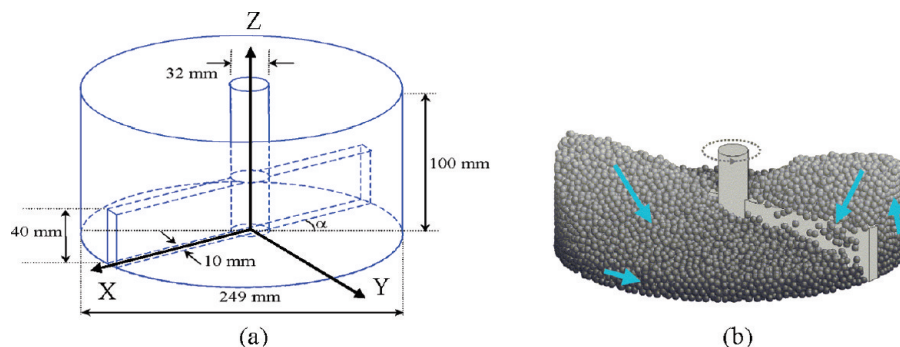


Figure 1. (a) Geometry of the mixer used in the simulation and (b) bed profile simulated at a blade speed of 20 rpm.

is followed by a gravitational settling process of about 0.95 s. The top surface of the packed particles roughly reaches the top edge of the blades, namely a height of about 40 mm from the bottom. The shaft–blade unit is rotated at a uniform angular velocity immediately after the settling process. A few blade rotations produce a macroscopically stable flow in the bed, and at this stage particle-scale or so-called microdynamic analysis is performed. The blade speed is varied between 2 and 100 rpm. The latter corresponds to a blade tip speed of 1.3 m/s, which is about 1/10 the blade tip speed required for a so-called high-speed mixer.¹¹ The drag force due to interstitial air has been neglected in the simulations, because the blade tip speed is still low, the inertia of particles is large, and the drag force is small.

It should be noted that the proposed DEM approach has been validated against the PEPT measurements as detailed by Stewart et al.¹⁰ The present work is just an extension of the previous studies,^{9,10} focused on the effect of rotational speed and based on the microdynamic information generated by DEM.

Results and Discussion

Flow Pattern. Examining flow patterns in a mixer is important because it enables us to identify mixing mechanisms or how the mixing is taking place in the mixer. Flow patterns in the mixer considered are quite complicated, although an angular motion can be observed dominantly. Following the treatments previously used,^{9,10} the motion of particles is here examined relative to the blades, in which the blades are imagined to be fixed while the particles are moving. The following general features can be observed in the flow patterns as shown by the arrows in Figure 1b: particles rise in front of the blade to form a heap; some particles flow downward on the heap surface in front of the blade and some flow over the blade; the particles that roll down to the front of the blade can rejoin the particle flow toward the blade. Similar particle motion has been found in the study of Stewart et al.,¹⁰ and more recently by Remy et al.¹⁴ in a four-blade mixer.

Internal flow fields can be analyzed by sampling at horizontal, vertical, or cylindrical sections.^{9,10} We use these methods to examine velocity fields present in the mixing process. In analyzing the velocity fields, we have used blade relative velocity, which is the velocity of a particle with respect to the frame of reference XYZ that rotates with the blade. In other words, the velocity vector $\omega \times \mathbf{r}$ is subtracted from the particle velocity vector, where ω is the angular velocity vector and \mathbf{r} is the position vector of the particle projected onto the horizontal plane. The blade relative velocity is used here because it represents the observation that most particles are engaged in angular motion. The blade relative velocities of the particles are normalized by the circumferential velocity of the blade tip.

Figure 2 shows the normalized blade relative velocities of particles in horizontal sections at three heights for four different blade speeds, where a sliced section contains the particles with center heights falling in the region between the section height ± 2.5 mm. In most sections, the blade relative velocities are clockwise because the blades are rotating anticlockwise. If the normalized blade relative velocity of a particle is close to unity, the particle can be considered as nearly at rest. Figure 2(i) shows the particle movements in section i, namely at the bottom part of the vessel at different speeds. At 2 rpm, particles close to the vessel wall are at rest or almost at rest as seen from Figure 2a(i). The particles in front of the blades have near-zero blade relative velocities, and therefore they are identified to be moving close to the blade speed, primarily in the direction of the blade rotation. The figure shows that the blade action is limited to

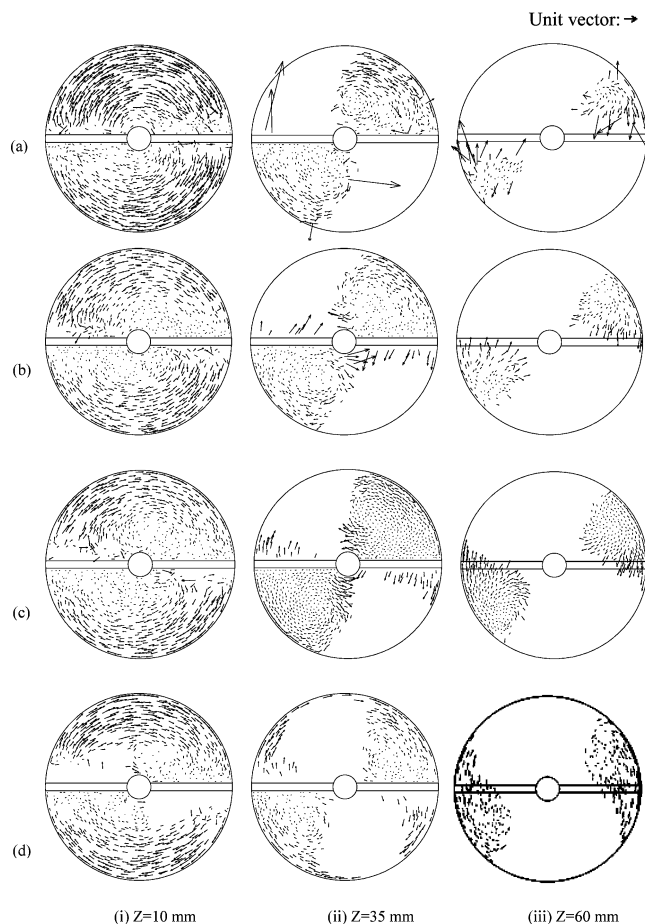


Figure 2. Instantaneous vector field of relative velocities of particles normalized by blade tip speed at three horizontal sections i, ii, and iii for four blade speeds. Row a is for 2 rpm at 130 s; row b is for 23.8 rpm at 55.3 s; row c is for 47.75 rpm at 27.5 s; and row d is for 100 rpm at 13.3 s; Z is measured from the bed bottom.

the neighborhood of the blade at 2 rpm. When the blade speed increases, blade relative velocities of the particles near the vessel wall decrease as shown in Figure 2b(i–iii); thus an increasing number of particles are being moved by the blade when the blade speed increases. In addition, higher blade speeds (47.75 or 100 rpm) produce a vortex (namely, circulatory motion of particles) in the corner of the shaft and leading blade surfaces. This vortex formation is also expected to contribute to the fast mixing at higher blade speeds. The faster the blade speed, the larger the empty space behind a leading blade as seen from Figure 2c(i),d(i).

Figure 2(ii,iii) shows particle movements at two more sections, namely, section ii at $Z = 35$ mm, which is just below the top of the blade, and section iii at $Z = 60$ mm. In section ii, circulatory motion of particles can be observed at all speeds. Relative to the blade, particles are moving very slowly from near the vessel wall toward the leading blade surface, and then toward the shaft, where they tend to rejoin the stream of particles moving toward the blade. When blade rotation speed is increased, the relative velocities of particles near the wall have reduced in this section, indicating that more particles are being forced to move by the blade. Similarly, with an increased blade speed, the number of particles going over the blade has also increased as seen from Figure 2c(ii),d(ii). These two factors contribute to a faster mixing rate at higher blade speeds. A few particles show large blade relative velocities at the slow speed of 2 rpm because of secondary particle collisions or gravity, producing larger normalized blade relative velocities than unity;

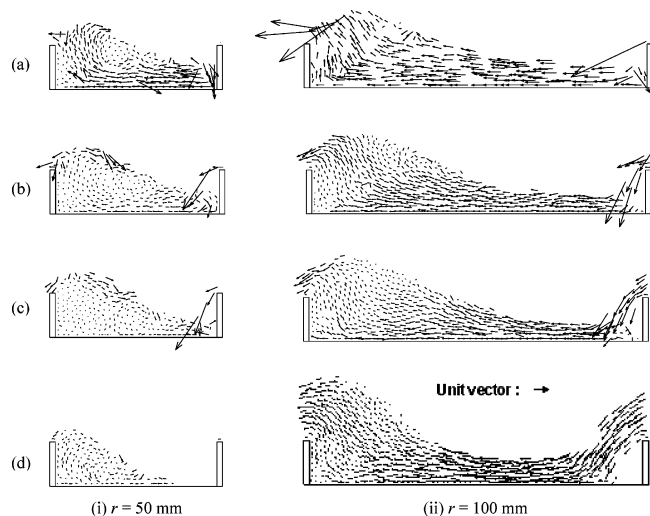


Figure 3. Normalized relative velocity fields in two cylindrical sections at $r = 50$ mm and $r = 100$ mm. Blade speeds and times (in rows) are, respectively, (a) 2 rpm and 130 s, (b) 23.8 rpm and 55.3 s, (c) 47.75 rpm and 27.5 s, and (d) 100 rpm and 13.3 s.

particles cannot gain a speed larger than the blade speed unless there is some energy transfer to the particles. Note that particles are not present behind the leading blades even at low blade speeds. In section iii, gravity-assisted movement of particles along the heap surface produces normalized relative velocities larger than unity. The number of particles going over the blade increases with increased blade speed. The particles still maintain a recirculating movement because of the transmission of tangential frictional forces from the particles below this section, where particles are in recirculating movement. In addition, the number of particles in the section has increased with the blade speed, meaning that the particle bed has increased its volume with increased blade speed.

Figure 3 shows the relative velocity fields in two cylindrical sections: namely, section i at radii $r = 50$ mm and section ii at $r = 100$ mm for the conditions of Figure 2. A cylindrical section starts from the vertical midplane of one blade and extends along a cylindrical surface up to the vertical midplane of the other blade. Note that the particle zones shown in Figure 3 can be considered as the region $Y > 0$ of Figure 1a. The cylindrical sections contain the particles whose centers are falling in the annular region defined by $r = R \pm 2.5$ mm, where R is the radius of section.

The flow in section i is representative of that near the shaft while that in section ii is representative of that closer to the mixer vessel wall. In section i, particle flow from the bottom of the mixer can be divided into two groups: one pushes particles over the leading blade and another forms a recirculating flow near the free surface of the heap. Particles rolling along the free surface of the heap and over the blades can have relative velocities larger than unity as discussed before. In section ii, particle flow is mostly unidirectional moving from right to left, except at low speeds, when a recirculating flow near the free surface can be observed. Particles undergo a velocity change as they move from right to left, initially slowing and then gaining velocity when they move over the blade.

The flow patterns observed at 2 rpm continue to exist at higher speeds. However, recirculating flow in section ii gradually diminishes with the increase of the blade speed. Conversely, in section i, complex regions of recirculating flows appear with the increase of the blade speed. Another effect of the increased blade speed is the increase of the height of the heap in front of

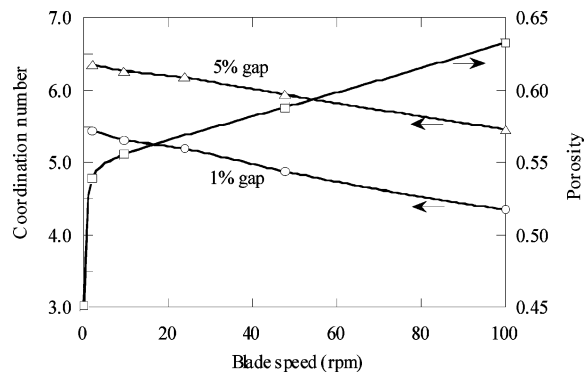


Figure 4. Coordination number (Δ) and porosity (\square) as a function of blade speed.

the blade, as observed by Stewart et al.¹⁰ Yet another effect of blade speed is the increase of the void space behind the blades when the blade speed increases, which was already mentioned in the discussion of Figure 2. The presence of a void space behind the blades has been observed experimentally at a blade tip speed of 1.4 m/s; the tip speed of the present work is 1.3 m/s at the rotational speed of 100 rpm.¹⁵

Flow Structure and Mixing Behavior. The flow structure of particles is examined in terms of the coordination number and porosity as used by Zhou et al.;⁹ both quantities are difficult to produce experimentally. The coordination number of a particle is defined as the number of particles that are in contact with the particle. The condition for particle contacts is defined as follows. A particle is in contact with another particle only if the gap or the clearance between the two particles is less than a certain value. Two gap sizes are considered here: 1% and 5% of the particle diameter. To obtain a statistical mean value for the coordination number at a given time, the coordination numbers of particles are arranged into a frequency distribution curve. The mean value of this distribution is then found by weighting the coordination number by its frequency: this gives the average value based on the number of data points. In counting the number of contacts, those with the blade surfaces and container surfaces have also been included. Although the coordination number is here obtained as an average value for the entire bed, porosity is calculated both as a local value and as an average value in the bed between two horizontally sliced sections.

Figure 4 shows the mean coordination number for the entire bed and porosity of the bed in the space between the bed bottom and top of the blade as a function of blade speed. The results show that the coordination number gradually decreases with increasing blade speed. On the other hand, the average porosity of the bed gradually increases with the blade speed. These results are consistent with the bed increasing in volume when the blade speed increases.⁹ The increase in the average bed porosity is drastic at low blade speeds, after which the increase is gradual with respect to speed. The coordination number does not show a drastic change in this speed range because it is not a local value, but an average over the entire bed.

DEM simulation records positions of all the particles in a system as a function of time, allowing us to quantify the mixing of the particles. To demonstrate the mixing action of the blades, the particles in the left and right halves of the vessel are colored by light gray and dark gray respectively before the start of mixing, as shown in column a in Figure 5. Columns b–d in Figure 5 show subsequent mixing states obtained from the DEM simulation, and rows i–iii correspond to different blade speeds. The images in the figure are for the cross section at a height of

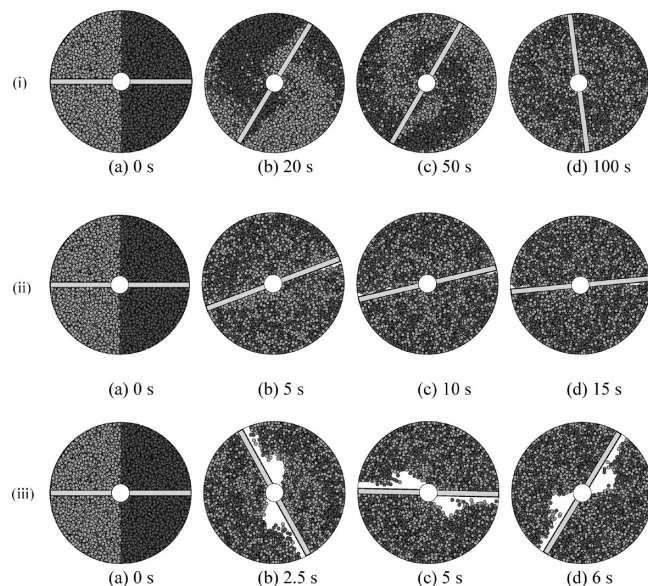


Figure 5. Mixing of dark and light gray particles initially arranged in the left and right halves of the mixer sliced at 37.5 mm height. Viewed from the top, when the blade rotates in anticlockwise direction at speeds of (i) 2, (ii) 47.7, and (iii) 100 rpm, with (a), (b), (c), and (d) representing elapsed time of mixing as indicated.

37.5 mm above the bottom of the vessel. Comparison of the sets of figures i, ii, and iii in Figure 5 shows that particles reach a well-mixed state (d) in gradually shortening time spans when the blade speed is increased. At 100 rpm, the leading blade is seen to have a void space behind it, which is a result of the particles moving upward in front of the leading blade, causing the particle bed to increase in height.

The quality of a binary mixture can be quantified by the variance of particle fraction p in the samples drawn from the mixture. If the sample variance of the mixture is small enough, the mixture can be considered to be well mixed or to have a good quality.¹⁶ The Lacey index M defined by eq 3 makes a comparison of the sample variance of the mixture S^2 with the variances S_0^2 and S_R^2 of the two reference states of the binary mixture, fully segregated and fully random states, respectively.¹⁷

$$M = (S_0^2 - S^2)/(S_0^2 - S_R^2) \quad (3)$$

The variance S_0^2 of the particle fraction of type 1 particles in a binary mixture at the fully segregated is given by $S_0^2 = pq$, where p is the particle fraction of type 1 particles in the mixture and $q = (1 - p)$ is that of the other type of particles in the mixture.¹⁶ p is roughly 0.5 for the case in Figure 5a. The variance S_R^2 of the particle fraction of type 1 particles in samples of size N taken from a fully random binary mixture is given by $S_R^2 = pq/N$.¹⁶ Note that the equation for S_R^2 is based on the assumption that the particles are different only in color and have a binomial probability distribution for position.¹⁶ The latter equation is not applicable to a binary mixture consisting of different sized particles, as implied by Kristensen's results on sampling by fixed volumes.¹⁸ The sample variance S^2 for the actual mixture is obtained by

$$S^2 = \sum_{i=1}^m \left[\frac{N_i}{N} \left(\frac{n_i}{N_i} - p \right)^2 \right] \quad (4)$$

Equation 4 represents the weighted average variance of the particle fraction n_i/N_i of type 1 particles n_i in the sample i of size N_i , and it accounts for the variation in the sample size; p is

the expected particle fraction of type 1 particles for the samples, m is the total number of samples, and N is the total number of particles in the mixture. Note that $\sum_{i=1}^m N_i = N$.

Evaluation of S^2 requires dividing the mixing space of the vessel into several axis-symmetric cells, each of which constitutes a sample. The division of the mixer space into cells is done as follows: (a) in the radial direction, the space between the shaft and vessel is divided into five annular sections of 21.7 mm width; (b) in the circumferential direction, the five annular sections are divided into 6, 11, 16, 21, and 26 segments from the innermost to outermost annular section respectively, with each segment in a section being of equal size; (c) in the axial direction, the circumferentially divided annular segments are then divided into cells of equal height of 20 mm from the bottom of the mixer. The samples produced according to the present segmenting method are different in size. However, this variation has been taken into account in eq 4; the resulting mixing index is reliable. This has been tested in our calculation of M under different conditions.

The effect of blade speed was investigated in our previous work,^{19,20} for blade speeds below 40 rpm. It was reported that the mixing index M of eq 3 collapses into a single curve when expressed as a function of the number of blade revolutions. Here the validity of this behavior is further examined in a larger blade speed range. Note that the two studies were conducted under the same conditions, except for the time step. In the previous work,^{19,20} the time step used was 50 μ s. In the present work, it was 5 μ s. The maximum acceptable limit is 54 μ s based on the known relationships for the particle properties considered.^{21,22} A smaller time step can generate more reliable results.

Figure 6a shows the mixing index M as a function of time and Figure 6b shows the mixing index M as a function of the number of revolutions at the four blade speeds; note that the x -axis of Figure 6b is a nonlinear transformation of the x -axis of Figure 6a. Figure 6a shows that the mixture reaches the fully mixed state, $M = 1$, in shorter times when blade speed is increased: namely, the rate of mixing increases with the blade speed due to increased convective flows, which is apparent from Figure 5. By contrast, Figure 6b shows that the mixing in terms of number of revolutions reaches the completely mixed state earlier at slow blade speeds than at fast blade speeds; at 2 rpm, $M = 1$ is reached in four revolutions compared to six revolutions at 100 rpm. M does not collapse into a single curve as previously observed, but rather it shows a speed dependence in the transition region of mixing. The results suggest that while the mixing due to convection is dominant, the mixing due to diffusion also plays a role, which results in varied relationships between M and the number of revolutions for a large range of blade speeds.

The observed speed dependence of M possibly results from the gradual increase in the bed porosity with faster blade speeds. The increased porosity will cause the total particle number in cells to decrease, which in turn will cause S^2 to increase as seen from eq 4. The increase in S^2 will result in a decrease in M as seen from eq 3. Other possible reasons for the decrease of M with the increased blade speed in the transition mixing region could be the loss of mobility of particles due to the increase of the energy loss in particle collisions and the increase of centrifugal forces on particles at higher blade speeds; the centrifugal effect cannot be ignored because the particle velocities are high as seen from Figure 2c(i),d(i) for the present mixer configuration. An analysis of the particle numbers in the cells also confirms that there is a redistribution of particles in the mixer once the blades start rotating, with the particle number

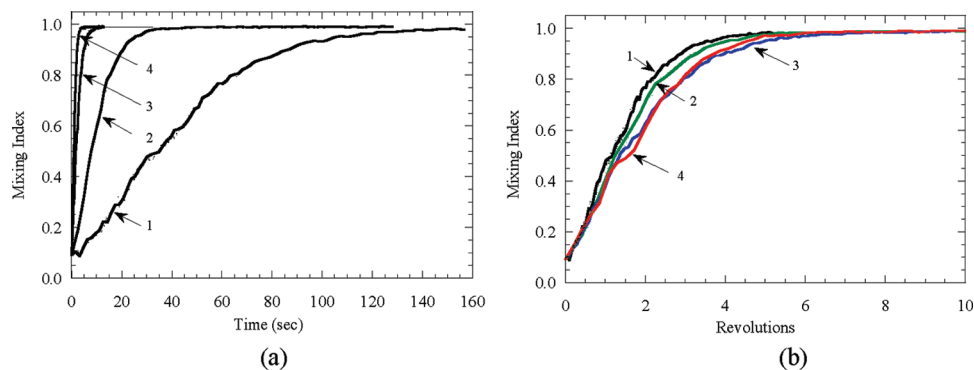


Figure 6. Mixing index as a function of time (a) and revolutions (b). Curves 1, 2, 3, and 4 represent blade speeds of 2, 9.55, 47.75, and 100 rpm, respectively.

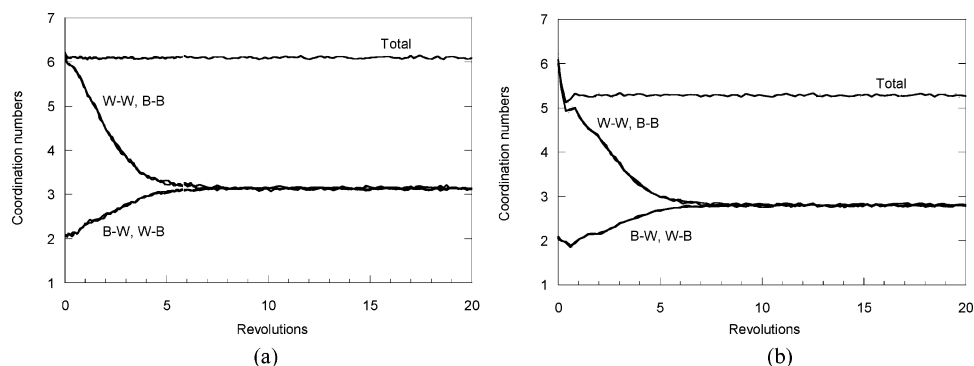


Figure 7. Variation of coordination numbers as a function of number of blade revolutions at (a) 10 and (b) 100 rpm.

near the vessel wall being increased, showing the effect of centrifugal forces. Both the increased energy loss and centrifugal forces make the particle movement relative to other particles more sluggish, or diffusive mixing becomes slower at higher blade speeds resulting in poor mixing in the transition mixing region; the diffusive action is generally known to become dominant from the middle part of a mixing curve.²³ M expressed as a function of the number of revolutions would help highlight the effects of diffusive mixing at different blade speeds; it shows that diffusive mixing can be delayed at high blade speeds due to increased centrifugal forces. Such a tendency should not be limited to only this type of mixer. In fact, poor mixing has been observed to occur at high speeds even in the case of a horizontal ribbon blender.²⁴ Therefore, it can be argued that increasing the blade speed is not a good practice for improving the mixing performance. Instead a better choice would be to increase the number of blades, which will allow us to reduce the blade speed while being able to achieve faster mixing. However, too many blades would give an opposite result because particles may not have chances to mix. Therefore, there may be an optimum number of blades for such a mixer. Figure 6b also shows that M slightly improves in the transition mixing region when the blade speed is increased from 47.75 to 100 rpm. This increase in M suggests a possible change of the mixing flow patterns or mechanisms with the increase of blade speed, and will be further discussed with reference to Figure 8.

To obtain changes in the coordination number with time, the particle bed at time $t = 0$ is divided into two halves by coloring the particles as in Figure 5a: the particles on the right side are colored black (B) and those on the left side are colored white (W). When the blade rotates, the particles move from one side to the other, and therefore the coordination number of each particle varies with time. A particle can have the contacts of the four different types, B-B, W-W, B-W, or W-B contacts,

at any instant in the mixing process. A frequency distribution can be found for each type by working through all the particles in the bed at any instant. Similarly, a frequency distribution can be found for the total number of contacts of each particle. The mean values of these frequency distributions are shown in parts a and b of Figure 7 as a function of time for 10 and 100 rpm, respectively. Note that the coordination numbers have been calculated on the basis that two particles are deemed to be in contact if the gap between them is less than $(5\%)d$, where d is particle diameter.

Initially, B-B and W-W contact numbers are both about 6. On the other hand, B-W and W-B contacts are both about 2. The fact that B-W or W-B contacts are not zero is due to the contacts at the interface between the segregated particles. Therefore, a particle will have about eight contacts under loose-packing condition at the beginning. The average of the total number of contacts (curves marked with "Total" in Figure 7) for a particle is however only slightly more than six; solid angle analysis shows that a single particle can have a maximum of 14 contacts with uniform-sized spheres in three dimensional space (N.B.: coordination number >12 is possible because of the $(5\%)d$ gap allowance used here). When the blade rotates, W-B and B-W contacts increase, while the B-B and W-W contacts decrease as seen from Figure 7 because of the particle movement. The contact number relationships for W-B and B-W contacts follow identical traces; so do those for W-W and B-B contacts. Such identical traces result from the fact that roughly equal numbers of particles are initially loaded in a side-by-side arrangement. In fact, a top-bottom particle arrangement of equal numbers of particles reveals the effect of vertical position. In about seven to eight blade rotations, all four curves reach the steady state, and their steady-state values are identical. Such identical steady-state values are a result of the two types of particles, B and W, being roughly equal. Figure 7

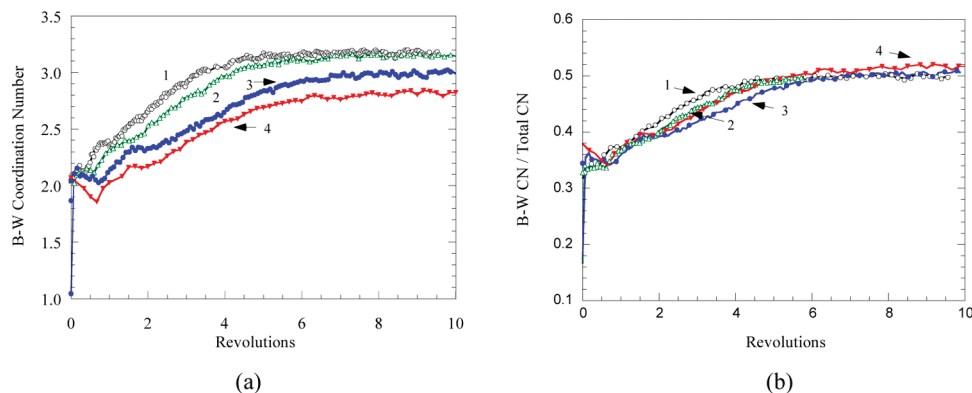


Figure 8. Effect of blade speed on the instantaneous average B–W coordination number (CN): (a) B–W CN as a function of shaft revolutions and (b) fraction of B–W CN to total average CN as a function of shaft revolutions. Curves 1, 2, 3, and 4 correspond to blade speeds of 2, 9.55, 47.75, and 100 rpm, respectively.

demonstrates the mixing occurring at a microscopic or particle scale as opposed to Figure 6, which shows the mixing occurring at a macroscopic or sample scale. Comparison of Figures 6 and 7 show that steady state is reached in roughly the same number of revolutions at macroscopic and microscopic scales.

A comparison of parts a and b of Figure 7 shows that the total coordination number has reduced at the steady state as a result of the blade speed being increased from 10 to 100 rpm. Although the total coordination number remains constant during the transient period of mixing, it shows a sharp reduction during the start-up process of mixing at 100 rpm. This reduction indicates that the bed has expanded when the blade moves from its stationary position. At 10 rpm, this reduction is not evident, but it is clear at higher speeds such as 47.5 and 100 rpm. Figure 7 also demonstrates that the bladed mixer is capable of homogenizing a mixture of monosized colored particles, although it has only a simple configuration.

Figure 8 shows the B–W coordination number (CN) as a function of blade revolutions at different blade speeds. It shows that the steady state of mixing is reached at a progressively larger number of revolutions when the blade speed is increased. This observation is consistent with the fact that diffusive mixing can be hampered by the increased centrifugal forces at larger blade speeds as observed in Figure 6b. Figure 8a shows that an increase in the blade speed results in a reduction in the steady-state value of B–W CN (see curves 1–4). This reduction is to be expected because the total coordination number decreases with the blade speed due to the bed dilation as shown in Figure 4. The fact that B–W CN has reached a constant value shows that mixing has reached the steady state at each blade speed, but it does not reveal the mixing state or the quality of the mixture. To examine the mixing states of the mixture, we use the fraction of the instantaneous averages of B–W CN and total CN as shown in Figure 8b. The results reveal that, in the transition period of mixing, the y value of Figure 8b, namely, the fraction of B–W contacts to the total number of contacts, decreases when the blade speed ω is increased from 2 to 47.75 rpm, but increases again when ω is increased from 47.75 to 100 rpm. This increase is probably caused by changes in the mixing flow pattern with the change in the blade tip speed: for 100 rpm, the blade tip speed is 1.31 m/s, while for 47.75 rpm, it is 0.62 m/s. It is known that when the blade tip speed is high, the particles move in a toroidal motion.^{11,25} The toroidal motion affects the profile of the particle bed near the cylindrical wall.²⁵ The changes in bed profile near the blade surface can be observed from Figure 11 (to be introduced later), when the blade

speed is increased. The bed profile in Figure 11d is typical of a toroidal motion.

The CN ratio of Figure 8b shows an increase in the steady-state value at 100 rpm. However, this increase does not imply that mixing has improved at that speed because the state of mixing at the steady state needs to be independent of the blade speed as seen from Figure 6. In other words, the mixer is only capable of fully randomizing the particles and cannot engage in increasing the quality of the mixture any further. Therefore, the observed slight increase in the steady-state value should have resulted from the use of the softer particles in this work. Use of a larger Young's modulus will have resulted in fewer particle deformations and thus fewer particle contacts, possibly reducing the B–W CN ratio at the steady state. Despite this issue, we can conclude from the particle-scale results that the use of the slow blade speeds produces a better mixing rate per blade revolution as seen from curve 1 of Figure 8b within the range of blade speeds of this study. The advantage of slow blade speed is further stressed from the viewpoint of the energy consumption in the section "Force Structure and Distribution".

In order to further investigate the flow near the cylinder wall at different rotational speeds in relation to particle mixing, we divided the annular section falling between $\theta = 0$ and $\theta = \pi$ and $r > 80$ mm into 15 equal cells in the circumferential direction, where θ is the angular position of a cell from the leading blade in the direction of rotation and r is the radius of the annular section. The average blade relative velocity of particles in each cell is evaluated at the steady state of mixing, and the velocity fractions V_z/V_θ and V_r/V_θ obtained. They are shown as a function of the circumferential position θ of the cells in Figure 9; here, V_r , V_z , and V_θ are the components of the average blade relative velocity for a cell in the radial, vertical, and circumferential directions, respectively. The shape of V_z/V_θ curves does not change much when the blade speed is changed in the range considered. However, the V_r/V_θ curve changes to a shape that clearly shows a minimum and a maximum at 100 rpm (curve 3), different from the lower speeds (curves 1 and 2) as seen from Figure 9b. Nilpawar et al.²⁵ reported sinusoidal shapes in the velocity ratios at a rotation speed of 312 rpm for a vessel having a diameter of 285 mm, where the blade tip speed will be 4.65 m/s. They described the motion of particles to be a toroidal motion, where the particles would rise near the wall and fall down toward the center. The Froude number Fr , defined as the ratio of centrifugal acceleration to gravity, $D\omega^2/(2g)$, is found to be 15.5 for their conditions. On the other hand, Fr is found to be 1.4 in the present work for

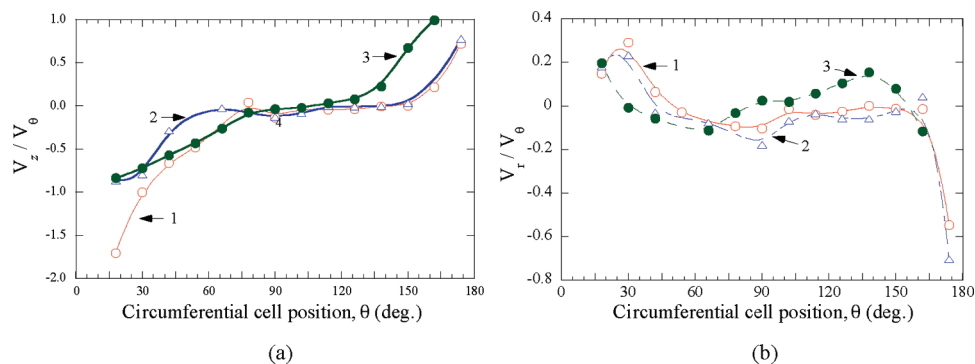


Figure 9. Variation of (a) V_z/V_θ and (b) V_r/V_θ for particles in the outer cylindrical section ($r > 80$ mm) as a function of the circumferential position θ at the steady state, where V_r , V_z , and V_θ are respectively the components in the radial, vertical, and circumferential directions of the average blade relative velocity of the particles in the localized section at θ . Curves 1, 2, and 3 correspond to the blade speeds of 9.55, 47.75, and 100 rpm, respectively.

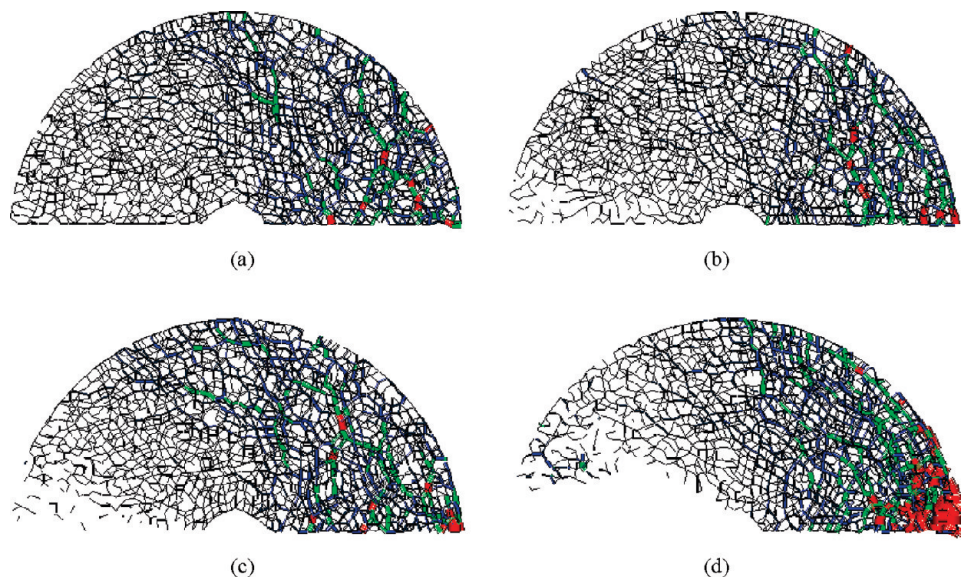


Figure 10. Normal force network in the horizontally sliced section of bed between $Z = 0$ and $Z = 10$ mm at four different blade speeds: (a) 2 rpm (at 5.24 rev); (b) 23.87 rpm (at 20.09 rev); (c) 47.75 rpm (at 21.88 rev); and (d) 100 rpm (at 21.66 rev). Color scale for the force, F : black, $F < 0.03$ N; blue, 0.03 N $< F < 0.1$ N; green, 0.1 N $< F < 0.2$ N; and red, $F > 0.2$ N.

a rotational speed of 100 rpm; by contrast, Fr is only 0.32 for a rotational speed of 47.75 rpm. Therefore, it can be argued that, at a rotational speed of 100 rpm, the centrifugal acceleration starts to become dominant overcoming gravity, resulting in a toroidal motion in particles. Therefore, the observed slight improvement in the mixing as seen from Figures 6 and 8 at macroscopic and microscopic levels when the rotational speed is increased from 47.75 to 100 rpm can be attributed to the change in the pattern of particle motion.

Force Structure and Distribution. To investigate the effect of blade speed on interparticle forces, we focus on force network diagrams and frequency distributions of the contact forces at different blade speeds. Contact force structure in a discrete particle system can be represented by a force network, where the magnitude of the normal contact force between two particles is represented by the thickness of a line joining the centers of the two particles.⁹

Figure 10 shows the force network diagrams in a horizontal sliced section of the bed between $Z = 0$ and $Z = 10$ mm at four different blade speeds, where Z is the height from the bed bottom. The diagrams show only half of the mixer ($Y \geq 0$ region of Figure 1), and the blade is rotating in the anticlockwise direction. In this section, normal contact forces propagate in the circumferential direction from the leading blade to the trailing blade, with a gradual reduction in magnitude in that

direction. At a low blade speed, the force chains are well connected in that direction as seen from Figure 10a. However, they tend to break up behind the trailing blade with increasing blade speed, as seen from the diagrams. The breakup of the force chains with the blade speed accompanies the appearance of increasingly larger void space behind the trailing blade as seen from the diagrams. Another observation is that force networks show a loose structure behind the trailing blade when the blade speed increases, indicating an increase in the volume of the bed. This observation is supported by a PEPT study by Stewart et al.¹⁰ By contrast, the force networks in front of the leading blade show a slightly tighter structure when the blade speed increases. Therefore, at all blade speeds, the normal contact forces are larger in the quarter of the mixer in front of the blade. When the blade speed is 100 rpm, large normal forces seem to shift toward the mixer wall in front of the blade, with the forces being in the range 0.1–0.2 N. This shift is due to the increase in the centrifugal forces on the particles when the blade speed increases.

Figure 11 shows the force network diagrams of normal contact forces for the conditions of Figure 10 in a vertically sliced section of the bed between $Y = 5$ mm and $Y = 55$ mm (see Figure 1). The figure confirms that large normal forces concentrate in the corner of the leading blade and the wall of the mixer. Particularly, large normal forces can be found at the

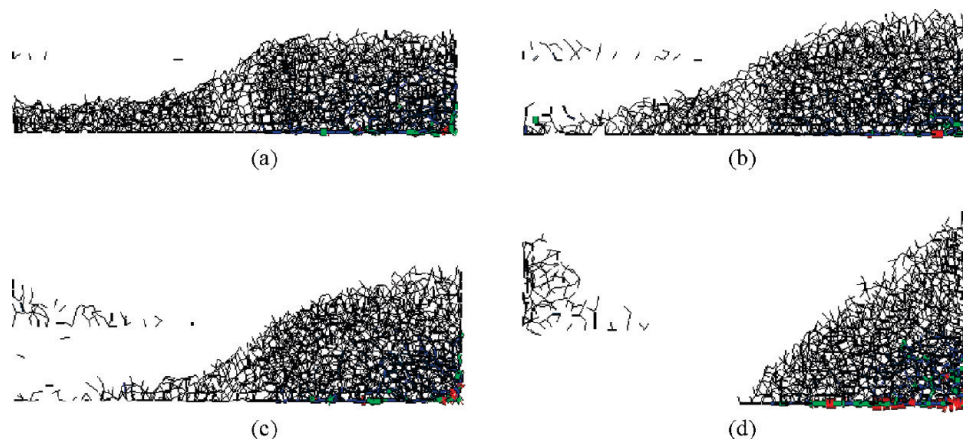


Figure 11. Normal force network in the vortice section passing through the leading blade surface: (a) 2 rpm (at 5.24 rev); (b) 23.87 rpm (at 20.09 rev); (c) 47.75 rpm (at 21.88 rev); and (d) 100 rpm (at 21.66 rev). Color scale for the force, F : black, for $F < 0.03$ N; blue, for 0.03 N $< F < 0.1$ N; green, for 0.1 N $< F < 0.2$ N; and red, for $F > 0.2$ N.

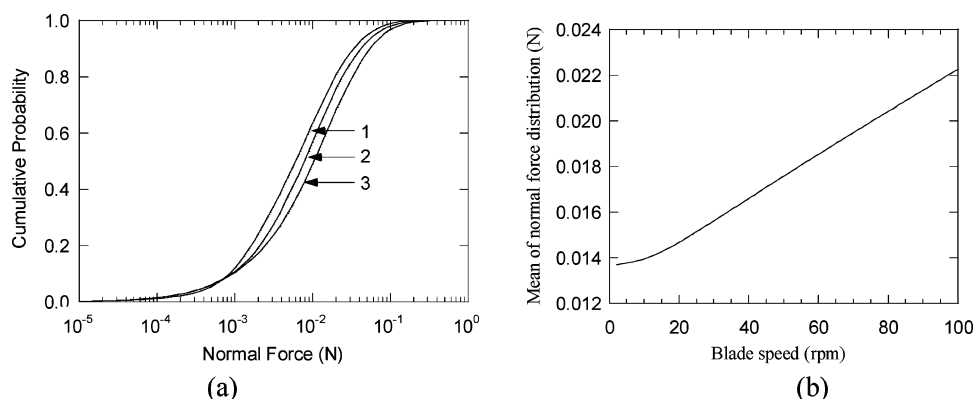


Figure 12. (a) Cumulative probability distributions of normal contact forces at different blade speeds: curves 1, 2, and 3 are for blade speeds of 2, 47.75, and 100 rpm, respectively. (b) Mean of the normal contact forces as a function of blade speed.

bottom of the mixer in this corner. Therefore, these forces can be reduced if the blade is lifted above the bottom of the mixer. Such a provision will help reduce particle breakage during mixing. The network diagrams also show that the particle profile in the vertical plane through the blade surface changes dramatically when the speed is increased. The heap height in front of the leading blade (on the right-hand side) increases, while that behind the trailing blade (on the left-hand side or LHS) decreases. The diagrams also confirm that the number of particles passing over the blade (on LHS) increases when the blade speed is increased because of the increased height of the heap in front of the leading blade. Note that the top edge of the trailing blade can be identified as an imaginary cutoff line on LHS of the diagrams, below which no particles exist. At 100 rpm, the particles build up twice as high as the blade height, which is 40 mm.

To be quantitative, Figure 12a shows cumulative probability distributions for the normal contact forces in the blade speed range 2–100 rpm. The normal forces can be identified to vary between 10^{-4} and 0.3 N in the speed range. The cumulative distribution curve is displaced toward a higher force range when the blade speed increases, implying that larger contact forces are present in the system at higher speeds. This increment in the normal contact forces can be observed from Figure 12b, which shows the mean values of the cumulative distribution curves as a function of blade speed.

A similar trend is observed for shear (tangential) forces at contact points. Figure 13a shows the cumulative probability

distributions for shear contact forces in the speed range 2–100 rpm. The shear forces can be identified to range between 10^{-4} and 0.1 N in the speed range. With an increase in the blade speed, the cumulative distribution is displaced to higher force range as with the normal contact forces, implying that larger shear forces are present at the contact points. This increment in the shear contact forces can be observed from Figure 13b, which shows the mean values of the cumulative distributions as a function of blade speed. By definition, the tangential force is proportional to the normal force between particles. It is therefore not surprising that Figures 12 and 13 are similar. The results in Figures 10 and 11 show that a zone of large interparticle forces is present in front of a blade near the bed bottom and that it moves toward the vessel walls at higher speeds. These are the regions where stress concentration occurs, possibly leading to particle breakage and severe attrition.

Figure 14 shows the simulation results of blade torque at the steady state as a function of the blade speed in the speed range 2–100 rpm. Zhou et al.⁹ have reported a torque of 1.1 N m at 10 rpm for the simulation conditions identical to those of this work. The torque becomes asymptotic at lower blade speeds and increases exponentially up to a blade speed of 100 rpm. However, it may be possible that the curve becomes linear with respect to the blade speed in the speed range 100–600 rpm as observed by Sato et al.²⁶ A good fit to these results can be represented by the exponential relationship $\Gamma = 1.086e^{0.0047\omega}$, where Γ is the blade torque (in N m) and ω is the blade shaft

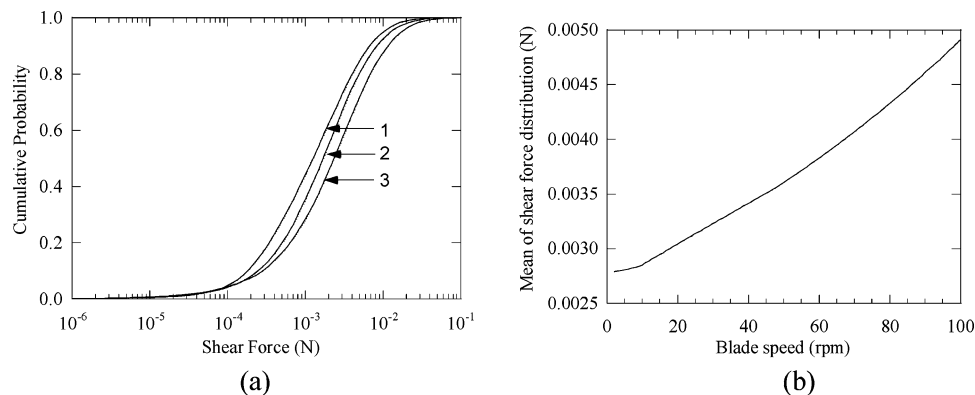


Figure 13. (a) Cumulative probability distributions of tangential contact forces at different blade speeds. Curves 1, 2, and 3 are for blade speeds of 2, 47.75, and 100 rpm, respectively. (b) Mean of shear contact as a function of speed.

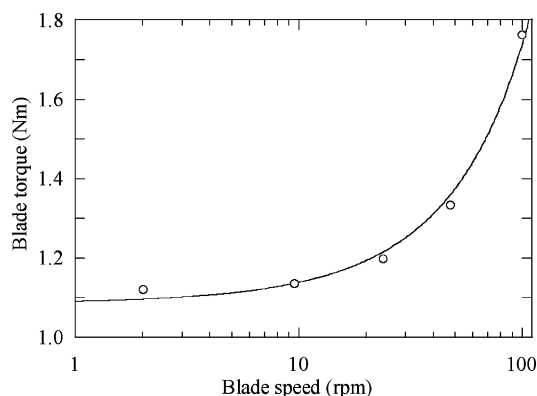


Figure 14. Steady-state blade torque as a function of speed.

speed (in rpm). This relationship predicts a torque of 1.086 N m at zero blade speed, which can be thought as the threshold torque required for the blade to move the particles in the mixer overcoming various frictional forces present.

Knight et al.¹¹ developed a semianalytical model for calculating the torque for mixing of powder in a vertical cylinder fitted with a shaft carrying flat vertical blades. They assumed the flow of powder to take place as a rigid body rotation, but incorporated in the model frictional and inertial interactions of the powder with blades. Although this model yielded a linear relationship between the torque and blade speed for powders, their experimental results show that the torque is exponential below roughly 200 rpm, but reduces to a linear form from around 600 rpm. The model is however not directly applicable here because it does not account for the particle size and empirical constants of the model are not known for this mixer configuration.

The energy consumed to achieve the fully mixed state $M = 1$ can be obtained on the basis of the information on mixing index and torque from Figures 6 and 14, respectively. Earlier, the blade speed of 2 rpm was observed to produce $M = 1$ in four revolutions compared to six revolutions required at a blade speed of 100 rpm. Although not shown here, the blade torque fluctuates around a mean value when the mixing proceeds at a constant blade speed, and therefore, the torque can be considered as constant at a constant blade shaft speed. The energy consumed at a given speed and time is thus simply the product of the torque on the shaft and the total angle swept by a blade from the start of mixing to the time considered. Thus, the energy consumed in four and six revolutions at 2 and 100 rpm respectively is 27.6 and 65.5 J, respectively; an energy saving

of 58% can be achieved by choosing 2 rpm over 100 rpm, though the mixing time increases by 33 times. When choosing higher blade speeds, another issue that should be addressed is the increase of heat generation, which also represents an energy loss.

Conclusions

DEM simulations were carried out to examine the influence of blade speed on mixing of spherical monosized particles in a cylindrical bladed mixer of vertical orientation. The influence was assessed in terms of a range of parameters related to flow, structure, and forces, such as flow fields in horizontal and cylindrical sections, coordination number, porosity, mixing index, force network in horizontal and vertical sections, interparticle forces, and blade torque. The following conclusions can be drawn:

(a) Viewed in the vertical plane through the leading blade, the bed profile changes drastically when the blade speed is increased. This profile shows that the heap height in front of the leading blade increases and that behind the trailing blade decreases drastically when the blade speed is increased. The increased heap height causes more particles to pass over a blade, and to form a void space behind the blade.

(b) Formation of a three-dimensional vortex can be observed in front of a leading blade close to the blade shaft, where the particles have a strong recirculating flow. The recirculating flows gradually diminish in both horizontal and cylindrical sections when the blade speed is increased. The recirculating flow close to the free bed surface disappears when the blade speed is increased, making the flow there mainly unidirectional.

(c) Coordination number variation captures the mixing process in the mixer. The variation shows a dilation in the particle bed at the start of mixing at high blade speeds, but it remains more or less the same in terms of average coordination number for the rest of the mixing process. Coordination number also shows a dilation in the flowing structure of particles with increasing blade speed in agreement with the porosity results.

(d) The rate of mixing is significantly enhanced by the blade speed as is evident from the shortening of the time taken to reach the steady state. However, the mixing rate per revolution shows a decrease in the transitional mixing region with an increase in the blade speed up to a certain speed, beyond which it shows again a slight improvement

in the transition region with the speed. This improvement can be attributed to the toroidal motion of particles in the mixer.

(e) In the speed range 2–100 rpm, normal contact forces at particle contact points are found to be in the range 10^{-4} –0.3 N. Tangential forces are found to be in the range 10^{-4} –0.1 N. Both are increased when the blade speed is increased. At higher speeds, large normal forces concentrate near the mixer wall in front of the blade due to an increase in centrifugal forces on particles. Generally, large normal contact forces concentrate in front of the leading blade at all blade speeds.

(f) In general, DEM can provide a description of the flow and force fields in a vertically shafted cylindrical mixer at the particle scale. It is now possible to readily and rapidly extend the approach to evaluate the effects of mixer geometry and operating conditions. Many of the effects due to particle size and cohesive force will also become equally accessible, enabling us to form methodologies for integrating scientific aspects with equipment design.

Acknowledgment

The authors are grateful to the Australian Research Council (ARC) for the financial support of this work.

Nomenclature

c_n = damping coefficient in the normal direction at a contact point
 c_t = damping coefficient in the tangential direction at a contact point
 D = mixer vessel diameter, m
 E = Young's modulus, Pa
 $\mathbf{F}_{cn,ij}$ = normal contact force vector between i and j , N
 $\mathbf{F}_{ct,ij}$ = tangential contact force vector between i and j , N
 $\mathbf{F}_{dn,ij}$ = normal viscous damping force vector between i and j , N
 $\mathbf{F}_{dt,ij}$ = tangential viscous damping force vector between i and j , N
 Fr = Froude number
 \mathbf{g} = vector of acceleration due to gravity, m/s^2
 I_i = moment of inertia of particle i , kg m^2
 m_i = mass of particle i , kg
 M = mixing index
 \mathbf{M}_{ij} = vector of rolling friction torque of particle i , N m
 $\hat{\mathbf{n}}$ = unit normal vector at contact point
 p = expected particle fraction of target particle type
 q = particle fraction of nontarget type particle in binary mixture,
 $q = (1 - p)$
 \mathbf{R}_i = position vector of contact point from the center of particle i , m
 S^2 = variance of particle fraction
 \mathbf{T}_{ij} = vector of rotational of rolling friction torque on particle i , N m
 \mathbf{V}_i = velocity vector of particle i , m/s
 \mathbf{V}_{ij} = relative velocity vector of particle j with respect to particle i at the contact point, m/s
 $\mathbf{V}_{n,ij}$ = vector component of \mathbf{V}_{ij} in the normal direction at the contact point of i and j particles, m/s
 $\mathbf{V}_{t,ij}$ = vector component of \mathbf{V}_{ij} in the tangential direction at the contact point of i and j particles, m/s
 V_r = component of the average blade relative velocity in a cell in the radial direction, m/s
 V_z = component of the average blade relative velocity in a cell in the vertical direction, m/s
 V_θ = component of the average blade relative velocity in a cell in the circumferential direction, m/s

Greek Symbols

δ_n = normal deformation between particles i and j , m
 δ_t = vector of accumulated tangential deformation between particles i and j , m
 $\delta_{t,\max}$ = maximum tangential deformation as defined as in Table 1 under nonslip condition, m
 μ_r = rolling friction coefficient, m
 μ_s = sliding friction coefficient
 ν = Poisson's ratio
 ω = speed of revolution of blade shaft
 $\boldsymbol{\omega}_i$ = angular velocity vector of particle i , rad/s
 $\hat{\boldsymbol{\omega}}_i$ = unit vector of angular rotation of particle i

Subscripts

0 = fully segregated state
 R = fully random state

Literature Cited

- (1) Bridgwater, J. Fundamental Powder Mixing Mechanisms. *Powder Technol.* **1976**, *15*, 215.
- (2) Bates, L. *User Guide to Segregation*; British Materials Handling Board Press: Cheshire, U.K., 1997.
- (3) McCarthy, J. J.; Shinbrot, T.; Metcalfe, G.; Wolf, J. E.; Ottino, J. M. Mixing of Granular Materials in Slowly Rotated Containers. *AIChE J.* **1996**, *42* (12), 3351–3363.
- (4) Bagster, D. F.; Bridgwater, J. The Flow of Granular Material over a Moving Blade. *Powder Technol.* **1969**, *3*, 323–338.
- (5) Malhotra, K.; Mujumdar, A. S.; Imakoma, H.; Okazaki, M. Fundamental Particle Mixing Studies in an Agitated Bed of Granular Materials in a Cylindrical Vessel. *Powder Technol.* **1988**, *55*, 107–114.
- (6) Parker, D. J.; Broadbent, C. J.; Fowles, P.; Hawkesworth, M. R.; McNeil, P. A. Positron Emitting Tracking. *Nucl. Instrum. Methods Phys. Res., Sect. A: Accel. Spectrom. Detect. Assoc. Equip.* **1993**, *326*, 592.
- (7) Broadbent, C. J.; Bridgwater, J.; Parker, D. J.; Keningley, S. T.; Knight, P. A Phenomenological Study of a Batch Mixer Using a Positron Camera. *Powder Technol.* **1993**, *76* (3), 317–329.
- (8) Cundall, P. A.; Strack, O. D. L. A Discrete Numerical Model for Granular Assemblies. *Geotechnique* **1979**, *29* (1), 47–65.
- (9) Zhou, Y.; Yu, A. B.; Stewart, R. L.; Bridgwater, J. Microdynamic Analysis of the Particle Flow in a Cylindrical Bladed Mixer. *Chem. Eng. Sci.* **2004**, *59*, 1343–1364.
- (10) Stewart, R. L.; Bridgwater, J.; Zhou, Y. C.; Yu, A. B. Simulated and Measured Flow of Granules in a Bladed Mixer. *Chem. Eng. Sci.* **2001**, *56* (19), 5457–5471.
- (11) Knight, P. C.; Seville, J. P. K.; Wellm, A. B.; Instone, T. Prediction of Impeller Torque in High Shear Powder Mixers. *Chem. Eng. Sci.* **2001**, *56*, 4457–4471.
- (12) Zhou, Y. C.; Wright, B. D.; Yang, R. Y.; Xu, B. H.; Yu, A. B. Rolling Friction in the Dynamic Simulation of Sandpile Formation. *Physica A* **1999**, *269*, 536–553.
- (13) Zhu, H. P.; Zhou, Z. Y.; Yang, R. Y.; Yu, A. B. Discrete Particle Simulation of Particulate Systems: Theoretical Developments. *Chem. Eng. Sci.* **2007**, *62*, 3378–3396.
- (14) Remy, B.; Khinast, J. G.; Glasser, B. J. Discrete Element Simulation of Free Flowing Grains in a Four-Bladed Mixer. *AIChE J.* **2009**, *55* (8), 2035–2048.
- (15) Kuo, H. P.; Knight, P. C.; Parker, D. J.; Adams, M. J.; Seville, J. P. K. Discrete Element Simulations of a High-Shear Mixer. *Adv. Powder Technol.* **2004**, *15* (3), 297–309.
- (16) Fan, L. T.; Chen, S. J.; Watson, C. A. Solids Mixing. *Ind. Eng. Chem.* **1970**, *62* (7), 53–69.
- (17) Lacey, P. M. C. Developments in the Theory of Particle Mixing. *J. Appl. Chem.* **1954**, *4*, 257.
- (18) Kristensen, H. G. Statistical Properties of Random and Non-Random Mixture of Dry Solids. *Powder Technol.* **1973**, *7* (5), 249–257.
- (19) Zhou, Y. C.; Yu, A. B.; Bridgwater, J. Segregation of Binary Mixture of Particles in a Bladed Mixer. *J. Chem. Technol. Biotechnol.* **2003**, *78*, 187–193.
- (20) Zhou, Y.; Yu, A. B.; Bridgwater, J. The Effect of Blade Speed on Granular Flow in a Cylindrical Mixer. Presented at The 4th World Congress of Particle Technology, Sydney, Australia, 2002.
- (21) Asmar, B. N.; Langston, P. A.; Matchett, A. J.; Walters, J. K. Validation Tests on a Distinct Element Model of Vibrating Cohesive Particle Systems. *Comput. Chem. Eng.* **2002**, *26* (6), 785–802.

(22) Tsuji, Y.; Kawaguchi, T.; Tanaka, T. Discrete Particle Simulation of Two-Dimensional Fluidized Bed. *Powder Technol.* **1993**, *77* (1), 79–87.

(23) Massol-Chaudeur, S.; Berthiaux, H.; Dodds, J. A. Experimental Study of the Mixing Kinetics of Binary Pharmaceutical Powder Mixtures in a Laboratory Hoop Mixer. *Chem. Eng. Sci.* **2002**, *57* (19), 4053–4065.

(24) Muzzio, F. J.; Llusa, M.; Goodridge, C. L.; Duong, N. H.; Shen, E. Evaluating the Mixing Performance of a Ribbon Blender. *Powder Technol.* **2008**, *186* (3), 247–254.

(25) Nilpawar, A. M.; Reynolds, G. K.; Salman, A. D.; Hounslow, M. J. Surface Velocity Measurement in a High Shear Mixer. *Chem. Eng. Sci.* **2006**, *61* (13), 4172–4178.

(26) Sato, Y.; Nakamura, H.; Watano, S. Numerical Analysis of Agitation Torque and Particle Motion in a High Shear Mixer. *Powder Technol.* **2008**, *186* (2), 130–136.

Received for review October 9, 2009

Revised manuscript received April 16, 2010

Accepted April 21, 2010

IE901581T